JPhys Energy



# The role of dopant segregation on the oxygen vacancy distribution and oxygen diffusion in CeO<sub>2</sub> grain boundaries

To cite this article before publication: Adam Symington *et al* 2019 *J. Phys. Energy* in press https://doi.org/10.1088/2515-7655/ab28b5

**IOP** Publishing Journal Title
Journal **XX** (XXXX) XXXXXX https://doi.org/XXXX/XXXX

# The Role of Dopant Segregation on the Oxygen Vacancy Distribution and Oxygen Diffusion in $CeO_2$ Grain Boundaries

**Adam R. Symington[1], Marco Molinari[2], Joel Statham[1], Ji Wu[1], and Stephen C. Parker[1]**

[1] Department of Chemistry, University of Bath, Claverton Down, Bath BA2 7AY, UK
[2] Department of Chemistry, University of Huddersfield, Queensgate, Huddersfield HD1 3DH, UK

E-mail: M.Molinari@hud.ac.uk, S.C.Parker@bath.ac.uk

Received xxxxxx
Accepted for publication xxxxxx
Published xxxxxx

## Abstract

An important challenge when attempting to identify the role of microstructure and the effect of dopant concentration on the properties of energy materials is to distinguish the behaviour of each grain boundary. In this paper we describe our recent work using atomistic simulations to investigate the structure, composition and oxygen transport of gadolinium doped cerium dioxide tilt grain boundaries. We find that energy minimisation can be systematically employed to screen grain boundary structures and dopant segregation. When dopants are distributed equally across grains, molecular dynamics simulations reveal oxygen vacancies reside near dopants, resulting in higher oxygen diffusivity. Once the dopants accumulate at the grain boundaries these grain boundaries become saturated with oxygen vacancies. We see fast oxygen diffusion within the grain boundary plane, although the depletion layer, as shown via the electrostatic potential appears to block transport across the grain boundary. However, this is highly dependent on the grain boundary structure as we find striking differences of the potential and the segregation behaviour between each of interface studied.

Keywords: space charge effect, space charge layer, electrostatic potential, grain boundary core, oxygen vacancy segregation, coincidence site lattice, grain boundary, ceria, cerium dioxide

## 1. Introduction

Fluorite structured ceramic materials, including ceria ($CeO_2$) and doped zirconia ($ZrO_2$), have attracted considerable attention for energy applications in the last three decades due to their high ionic conductivity. [1, 2] These ionic conductors find use as solid electrolytes in solid state electrochemical devices such as solid oxide fuel cells (SOFC). [3-5] However the widespread use of such devices is hindered by material issues relating to high operating temperatures. [6] Lanthanide doped ceria materials, i.e. $Ln^{3+}$ ions like gadolinium, exhibit excellent oxygen conductivity due to the introduction of excess ionic carriers (oxygen vacancies). These doped materials, particularly gadolinium doped ceria (GDC), allow for slower material degradation as the diffusion of oxygen occurs at lower operating temperatures (600˚C - 800˚C), [6-8] with further improvement obtained through a reduction of particle size. [9, 10] Thus demonstrating that the microstructure plays a key role in the material properties.

Polycrystalline GDC, similar to other doped oxides, shows defect segregation to the grain boundaries (GBs), which has been observed experimentally and is detrimental to material properties. [11, 12] As defects, particularly



 

dopants, segregate and accumulate at the GBs, they may contribute to an increase in grain boundary resistance to the transport of oxygen. This results in a reduction in the conductivity of polycrystals compared to single crystals. [12-15] It is therefore critically important to understand and ultimately control the processes that occur at these interfaces and how they affect the materials properties.

The degradation associated with dopant segregation at grain boundaries in GDC has been studied theoretically to elucidate the atomistic details relating to the mechanism.[16] A hybrid Monte Carlo-molecular dynamics (MD) revealed that $Gd^{3+}$ segregation to the GBs is a thermodynamically favourable process, [17] and driven by a high oxygen vacancy concentration at the GBs. However, this study was only limited to the Σ5(310)/[001] tilt grain boundary in GDC. Dholabhai et al. combined MD and density functional theory to study three symmetric GDC GBs, namely theΣ3(111)/[110] tilt GB, Σ5(310)/[001] tilt GB and Σ5(001) θ=36.87◦ twist GB, [18] finding that GBs have different segregation behaviour, and that the stability of dopant-vacancy clusters at GBs was heavily dependent on the local structure and dopant arrangements at the GBs.

This work builds on our previous work on dopants in $UO_2$[19] but has been expanded to consider the effects of dopant distribution, dopant concentration and given the importance of space charge effects in $CeO_2$[9, 14, 20, 21], the change in electrostatic potential at grain boundaries. We present a survey of different coincidence site lattice grain boundaries in stoichiometric ceria and GDC with gadolinium concentration between 10% and 30%. We have considered multiple dopant distribution schemes, specifically, a uniform distribution symptomatic of freshly made devices, and a configuration with full $Gd^{3+}$ segregation at the grain boundary symptomatic of degraded devices. The stability, dopant and oxygen vacancy segregations, electrostatic potential along with the oxygen diffusivity of these grain boundaries are evaluated as a function of temperature and dopant concentration.

## 2. Methodology

Grain boundaries of $CeO_2$ were constructed using the METADISE code [22] with a classical potential model based on rigid ions and partial charges according to

$$U(r) = D_{ij}\left[\left\{1 - e^{-a_{ij}(r-r_0)}\right\}^2 - 1\right] + \frac{C_{ij}}{r^{12}} \qquad (2.1)$$

where $D_{ij}$ is the depth of the potential energy well, $a_{ij}$ is the a function of the slope of the potential energy well, $r$ is the distance of seperation, $r_0$is the equilibrium distance between species i and j, and $C_{ij}$ relates to the potential energy well and describes the repulsion at very short distances between species i and j. The parameters used for each species, reported in Sayle et al., are shown in Table 1[23].

**Table 1 –** Potential parameters

| Species | $D_{ij}$ (eV) | $a_{ij}$ (Å$^{-2}$) | $r_0$ (Å) | $C_{ij}$ (eV Å$^{12}$) |
|---|---|---|---|---|
| $Ce^{2.4}$-$O^{-1.2}$ | 0.098352 | 1.848592 | 2.930147 | 1 |
| $Gd^{1.8}$-$O^{-1.2}$ | 0.028451 | 2.057296 | 3.074956 | 3 |
| $O^{-1.2}$-$O^{-1.2}$ | 0.041730 | 1.886824 | 3.189367 | 22 |

This model has been shown to accurately reproduce the structural and elastic properties of $CeO_2$ and $UO_2$.[24, 25] Grain boundary structures were generated initially by taking each possible surface termination comprised of surface unit cells with no dipole perpendicular to the surface and scanning one surface relative to the other [26]. At each grid point in this scan a full surface relaxation is performed and as an extension to earlier approaches the lowest energy structures were then annealed across a wide temperature range using molecular dynamics.

Grain boundary formation energies without taking temperature effects into account, were calculated according to

$$\gamma_{GB} = (E_{GB} - E_{Bulk})\,/2A \qquad (2.2)$$

where E_GB and E_Bulk are the energies of the GB and bulk simulations cells respectively and A is the area of the GB plane.

Defect incorporation energies were investigated for the six grain boundaries using the CHAOS code, [27] namely $Gd^{3+}$ substitution at $Ce^{4+}$ sites and oxygen vacancies ($V_o$ ). This approach employs the Mott-Littleton method to evaluate point defect energy at every site in the simulation cell. It has the advantage of including both the electrostatic and steric contributions by including a full relaxtion. Defects were incorporated at every site into each boundary, which corresponds to the grain boundary plane and extended to a depth of approximately 30Å perpendicular to the boundary, in order to map the energetics of the defect as a function of their distance from the GB. Defects were considered to be point defects. ). The energies are presented with reference to the bulk defect energy which is set to 0 eV.

All molecular dynamics (MD) simulations were performed using the DL_POLY code. [28] Simulations of 4 ns employed 3 dimensional periodic boundary conditions, a timestep of 1 fs, an 8.5Å cut-off, within a temperature range of 900 – 3000 K, at intervals of 300 K. Equilibration was performed for 1ns using the NPT ensemble until unit cell volume was converged. Production simulations were carried out for 3ns using the NVT ensemble with a Nose-Hoover

thermostat. All grain boundary structures were annealed at high temperature and then cooled down to low temperature using the NPT MD ensemble. The annealing allowed for the most stable structure across the wide temperature range of each grain boundary to form.

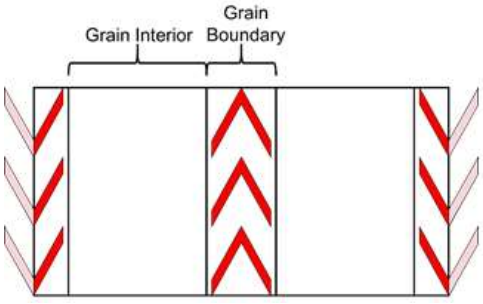


Figure 1: Schematic illustration of the model configuration for grain boundary configuration. Two grain boundaries run parallel in opposite directions.

Figure 1 shows a schematic representation of the simulation cells and Table S2 presents the size of the simulation cells for MD simulations, typically 7500 atoms. The grain boundary is sandwiched between grain interiors forming a layered structure and grain boundaries are far apart to avoid interaction. The grain boundary widths, represent the grain boundary region either side of the grain boundary core. The grain boundary width is the region of the structure that contains the grain boundary and extends until the diffusivity returns to the bulk value.

We generated configurations with fully segregated $Gd^{3+}$ (represented a degraded SOFC device) and configurations with $Gd^{3+}$ distributed randomly (representing a freshly prepared device) for investigation with molecular dynamics. Stoichiometric structures were also simulated as a control, referred to as CO. Three concentration of $Gd^{3+}$, 10%, 16% and 30% were substituted to $Ce^{4+}$ cations. These percentages represent the concentration of dopants over the overall number of $Ce^{4+}$ cations in the simulation cell. Different doping schemes where studied; N_GB – $Gd^{3+}$ doped $CeO_2$ nanolayered structures with N% random substitution of $Gd^{3+}$ localized within the grain boundary regions; e.g. 10_GB represents a configuration with 10% $Gd^{3+}$ randomly distributed within the grain boundary regions. N_Rand – $Gd^{3+}$ doped $CeO_2$ nanolayered structures with N% substitution of $Gd^{3+}$ randomly distributed through the entire structure, i.e. grain interior and grain boundary region; e.g. 10_Rand represents a configuration with 10% $Gd^{3+}$ randomly distributed within the entire structure. We note that 30_GB cannot be formed within our model as there are not enough $Ce^{4+}$ cations within the grain boundary regions to accommodate 30% $Gd^{3+}$ substitution. Oxygen vacancies were introduced randomly to maintain charge neutrality throughout the entire structure, however their distribution is not a concern as their mobility is such that they reached their equilibrium distribution within the NPT MD simulation. This was confirmed by examining the evolution of the oxygen stoichiometry over time. Oxygen vacancies segregated during the early stages of the NPT simulation and this distribution persisted for the duration of the simulation. Diffusion data for O within a specified region was obtained from a regional mean squared displacement (MSD) within the region of interest according to

$$\langle r_i^2(t)\rangle = 6D_O t, \qquad (2.3)$$

where $\langle r_i^2(t)\rangle$ is the MSD, $D_O$ is the diffusion coefficient for oxygen, and t is time. The calculation of the MSD only takes into account those segments of atom trajectories for oxygen species that pass within the region of interest e.g. the grain boundary.

We use the residence time τ to evaluate the average time that an oxygen atom spends in contact with each cation ($Ce^{4+}$ and $Gd^{3+}$ ) [29]. The τ was calculated from the residence time correlations function, which is defined as

$$\langle R(t)\rangle = \langle \frac{1}{N_0}\sum_{i=1}^{N_t}\theta_i(0)\theta_i(t)\rangle, \qquad (2.4)$$

where N is the number of oxygen atoms within a 3Å radius of the cation and $\theta_i(t)$ is the heavyside function, which is 1 if the ith oxygen atom is in the 3Å radius at t and 0 otherwise. An oxygen atom was only considered to have left the 3Å radius if it did so for at least 2 ps, which allowed molecules that temporarily left then re-entered to be included in τ . Equation 2.4 is integrated to calculate τ .

$$\tau_r = \int_0^\infty R(t)dt. \qquad (2.5)$$

The electrostatic potential in one dimension across the grain boundary was calculated according to

$$\Delta_\varphi(x) = -\int_{x0}^{x} E(x)dx, \qquad (2.6)$$

where $E(x)$ is the electric field and given by

$$E(x) = \frac{1}{-\varepsilon_0}\int_{x0}^{x}\rho_q(x)dx \ , \qquad (2.7)$$

where $\rho_q$ is the total charge density perpendicular to the interface and $\varepsilon_0$ is the permittivity of free space [30].

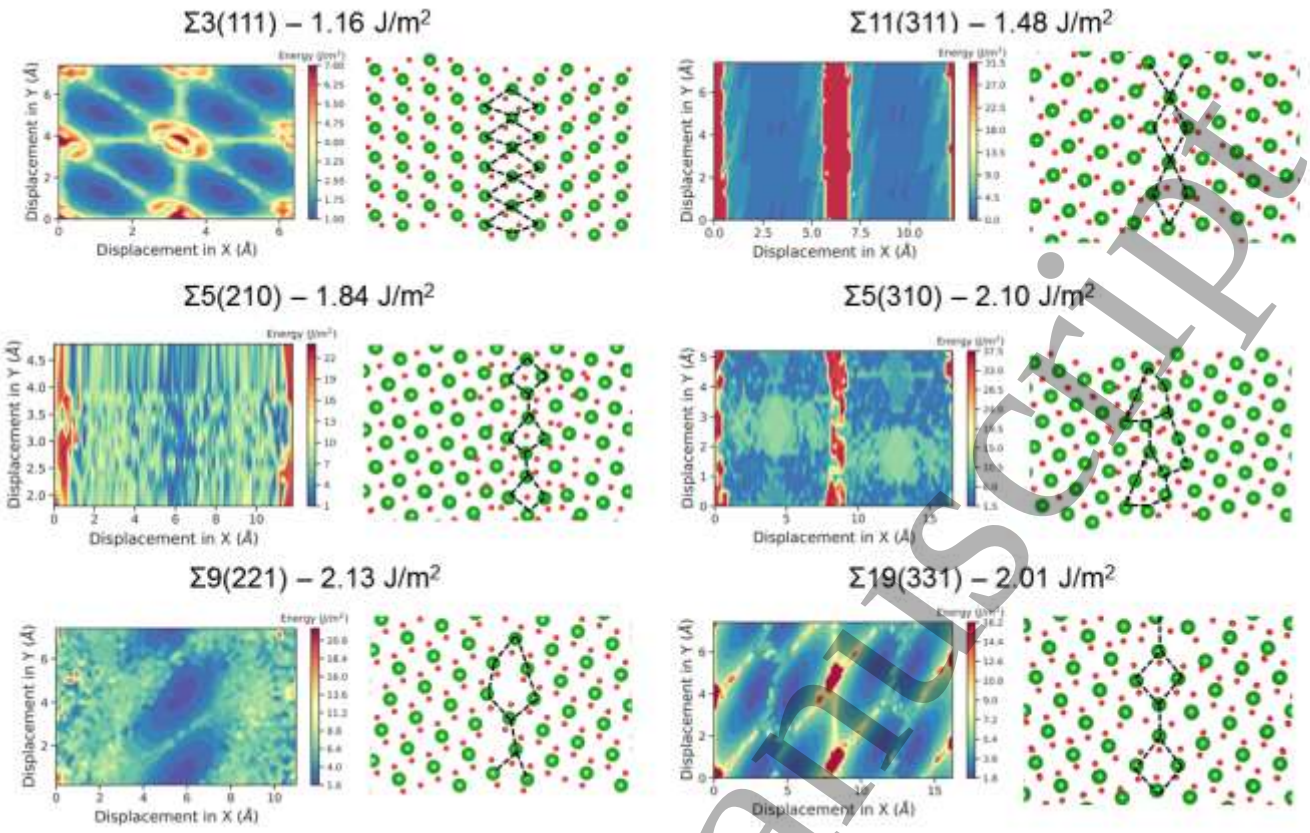


Figure 2: Potential energy surfaces and the lowest energy grain boundary configurations for each grain boundary studied. Red and green regions on the energy surface correspond to regions of high and low GB formation energy. In the structures, oxygen and cerium atoms are shown in red and green. Grain boundary energies are also shown.

## 3. Results

### *3.1 Stoichiometric Grain Boundary Structures and Potential Energy Surfaces*

The GB structures used in this study and their scans are presented in Figure 2. These were choosen from a database of different tilt grain boundary scans generated during this study (Figure 3). These six tilt grain boundaries are low Miller index surfaces with low formation energies. The Σ3(111), Σ5(210), Σ5(310), Σ9(221), Σ11(311) and Σ19(331) boundaries have all been observed experimentally, suggesting they are low energy and are present in significant concentrations within polycrystalline fluorite samples. [31-34]. The scans relate to the symmetry of the surfaces and enables us to infer the energy barriers to processes such as grain boundary sliding and also the depth of the energy well, which reflects the likelihood of the boundary forming.

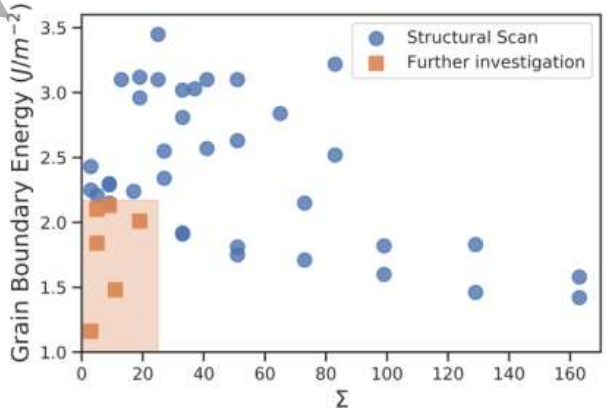


Figure 3 – Grain boundary energies calculated from the grain boundary scan method outlined above. For clarity, blue dots denote GB energies calculated during the structural scan and orange dots denote the GB energies of the boundaries investigated further in this study. The high Σ values refer to (hkl) where $h \leq 9$.

### *3.2 Dopant Segregation Energy at Grain Boundary*

Once the most stable structure of a specific GB is found, point defect segregation energies were calculated. Figure 4

shows the defect segregation energy profiles for the Σ19(331) grain boundary as example, with the rest being included in the SI (Figure S1). In all cases, the grain boundary regions (defined from -15 Å to 15 Å with the grain boundary core at 0Å ) were found to be energetically favourable to accommodate both $Gd^{3+}$ and oxygen vacancies ($V_o$ ) (0.15 - 0.2 eV per defect) , which is in agreement with previous computational work on specific GB structures. [17, 18] Although most sites are energetically favourable for a defect to segregate, some specific sites within the GB region were calculated to have slightly higher energies with respect to energies of defects located in the bulk regions outside of the grain boundary. This behaviour implies that segregation of dopants is site dependent within a specific structure and will be missed if considering only average properties of each plane of atoms.

We have also used molecular dynamics simulations to evaluate the impact of temperature and dopant concentration on the energetics of Gd segregation.

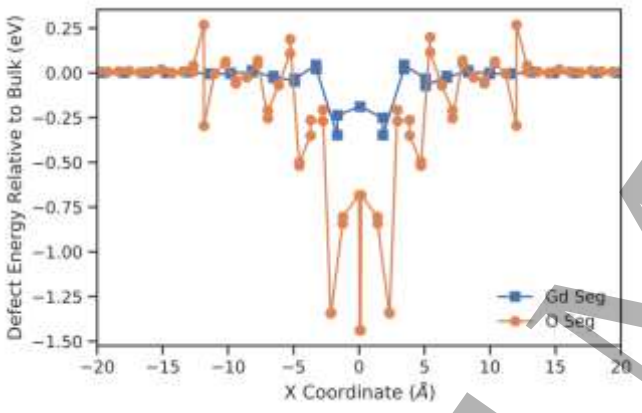


Figure 4: Relative defect energy profile for the Σ19(331)(A) grain boundary in $CeO_2$ with a single point defect. The grain boundary region exists between -15 Å- +15 Å and the grain boundary core is at 0 Å.

In this case by comparing the N_GB models where all the dopants are in the GBs, to the N_Rand models where $Gd^{3+}$ dopants are randomly distributed throughout the entire structure. The difference in configurational energy between the two N_GB and N_Rand configurations (10% and 16% concentrations) is shown in figure 5. The data indicates that the energetic contribution favours $Gd^{3+}$ segregation at the GBs rather than random distribution in all models evaluated. This is in line with experimental evidence [32, 35] and is supported by our defect segregation energies, which neglect temperature (Figure 4 and Figure S1). Increasing temperature increases segregation energies until about 2700K, beyond which the grain boundaries start to melt.

### *3.3 Doped Grain Boundary Structure*

On random introduction of $Gd^{3+}$ ions over the entire simulation cell (N_Rand) the stoichiometric grain boundary structures are retained. However, when $Gd^{3+}$ was segregated within the grain boundary regions (N_GB), there are significant structural rearrangements during the annealing (Figure 6). The Σ3(111) grain boundary undergoes a shift parallel to the grain boundary plane with the cation arrays converging into the middle of the grain boundary pipes. The presence of impurities promotes an alteration to the structure of the Σ5(210) with similar structural changes previously reported for stoichiometric $UO_2$, [25] but not yet for GDC. However previous studies on $Gd^{3+}$ segregation in GDC grain boundaries are based on a static model of un-doped $CeO_2$, [17, 18] where the composition of GDC is considered to be a dilute solution of point defects and temperature is neglected. We recognise that the concentration of Gd in the N_GB models is relatively high, thus may not be representative of many experimental studies. However our results are the first that show that high concentrations of Gd can cause an alteration in grain boundary structure, which may impact those experimental sample of doped nanoceria with high concentration of Gd[10].

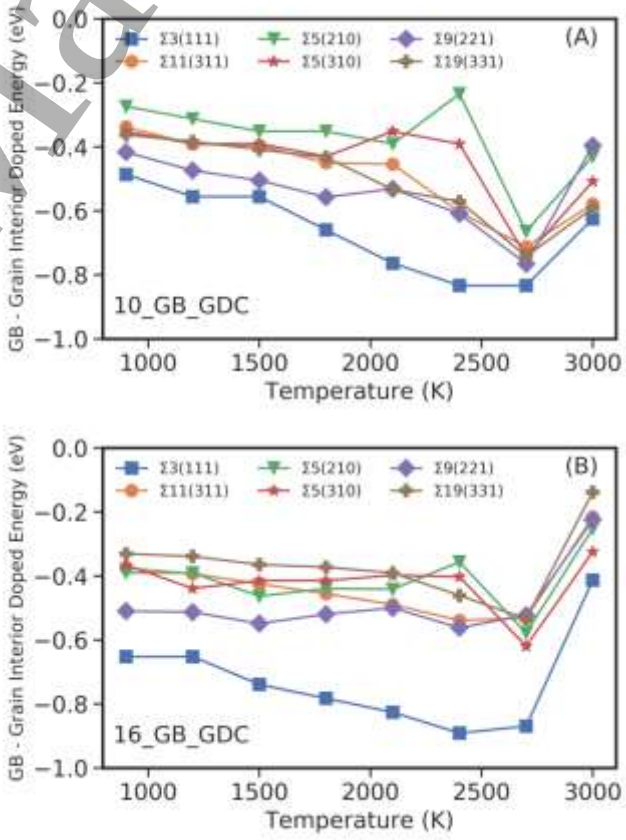

Figure 5: Energy difference between the 10_Rand and 10_GB (A) configurations and 16_Rand and 16_GB (B) configurations per $Gd^{3+}$ ion.

A possible explanation for these structural rearrangements is that the dopants stabilise metastable grain boundary configurations at higher temperatures, which may be energetically inaccessible under stoichiometric conditions, although these structures may be present in the potential energy surfaces presented in Figure 3. It is worth noting that the GDC material is used at relatively high temperatures (600K - 1000K or higher)[36] in thermochemical devices, thus the GB structures are likely to change over time. Therefore, the segregation triggered structural transformations is likely to be important in the study of the long-term degradation behaviour of GDC.

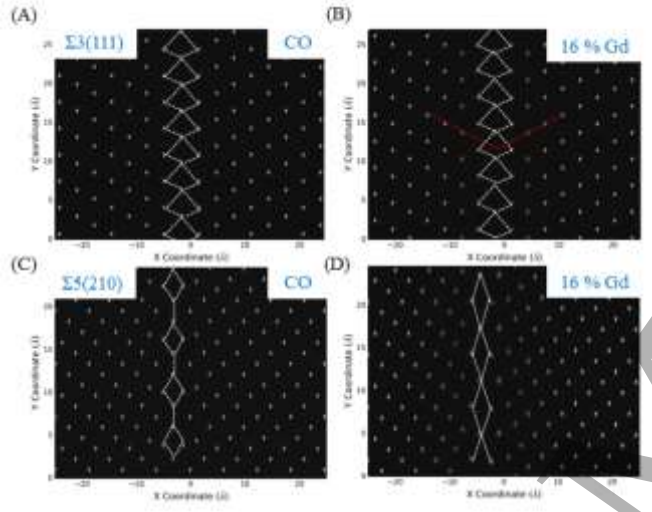


Figure 6: Time averaged 2D density profiles of the centre of mass of the cations ($Ce^{4+}$ /$Gd^{3+}$ ) displayed every 0.5ps at 2100 K for the stoichiometric and 16 GB Σ3(111) and Σ5(210) structures. The white dots denote the cation arrays parallel to the grain boundary plane. Patterns have been drawn to aid visibility.

### *3.4 Oxygen Vacancy Segregation at Grain Boundaries*

We have quantified the distribution of oxygen vacancies ($V_o$) within the doped configurations as the $V_o$ concentration within the two regions per $Å^3$ i.e. the grain interior (GI) and the grain boundary (GB) regions (Figure 7). In the N_GB, there is almost complete depletion of $V_o$ in the grain interior region and complete segregation of $V_o$ to the GB region. In all N_Rand configurations, where the $Gd^{3+}$ concentration is constant with depth, there is still a small increase in the concentration of $V_o$ per $Å^3$ at the grain boundaries. Thus indicating that while the dopants strongly attract oxygen vacancies, there is still a contribution from the grain boundary. If the GB structure was not a driving force for $V_o$ segregation, then we would have seen an equal or greater concentration of $V_o$ in the GI region of the N_Rand configurations. In effect, in the N_Rand configurations, the grain boundary and the dopant $Gd^{3+}$ in the grain interior are in competition for oxygen vacancies.

The average cation-oxygen coordination number (CN) within the first coordination shell (3 Å from the cation) as a function of temperature (Figure 8C/D) show that $Ce^{4+}$ is surrounded by a greater number of oxygen ions on average compared to $Gd^{3+}$ . This is a common feature within the grain boundary structures, doping schemes and configurations studied. This is evidence that there is a stronger interaction between $Gd^{3+}$ and $V_o$ compared to $Ce^{4+}$ and $V_o$.

The formation of this first nearest neighbour $Gd^{3+}$ - $V_o$ clustering has been reported in the literature [37] for bulk cerium dioxide. For the N_Rand configurations, the oxygen CN of $Ce^{4+}$ , either in the grain interior or in the grain boundary, decreases as the concentration of $Gd^{3+}$ increases from 10 to 30%. The oxygen CN of $Ce^{4}$+ in the grain boundary region of N_GB configurations follows the same trend, although the difference between 10% and 16% $Gd^{3+}$ doping is less prominent. The same pattern applies to the oxygen CN of $Gd^{3+}$ in both N_Rand and N_GB configurations, which is due to the decrease of the total oxygen ions available in the simulation cells.

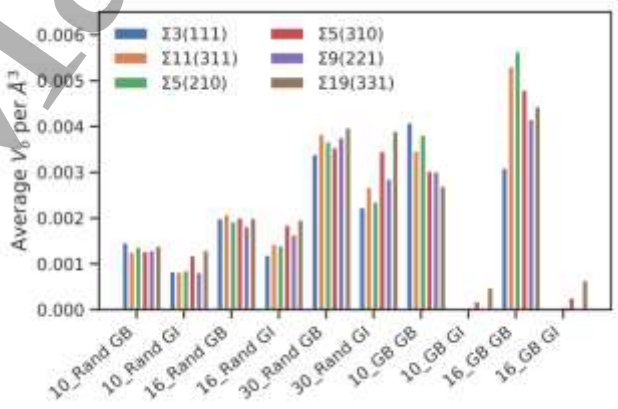


Figure 7: Oxygen vacancy distribution within the grain interior (GI) and GB regions of each configuration at a representative temperature of 2100 K. The full dataset across the temperature range studied can be found in the SI.

We also used residence time analysis, i.e. the average time spent by an oxygen atom within the first coordination sphere of a cation, to define the preferential affinity to oxygen with $Ce^{4}$+ or $Gd^{3+}$ . On average, we find that oxygen resides longest closer to $Ce^{4+}$ than $Gd^{3+}$ (Figure 8A/B). This supports the stronger interaction between oxygen vacancies and $Gd^{3+}$. The residence time decreases with increasing temperature as the diffusion of oxygen becomes more predominant. At high

temperature the residence time for both $Ce^{4+}$ and $Gd^{3+}$ converge to the same value. It is also evident from our data that all the grain boundaries, i.e. extended defects, behave in a similar way, and have a marginal effect on the time oxygen resides close to a cation, i.e. for $Gd^{3+}$ a point defect. Based upon these observations and our defect segregation energies (Figure 4), we infer two key points. First, there is a strong interaction between $Gd^{3+}$ and $V_o$, which causes oxygen vacancies to distribute partially due to the distribution of the $Gd^{3+}$. This is not surprising given that the effective charges of $Gd^{3+}$ and $V_o$ are -1 and +2 respectively. Secondly, grain boundaries themselves have a strong interaction with oxygen vacancies and cause some $V_o$ to segregate to the boundary despite uniform distributions of $Gd^{3+}$.

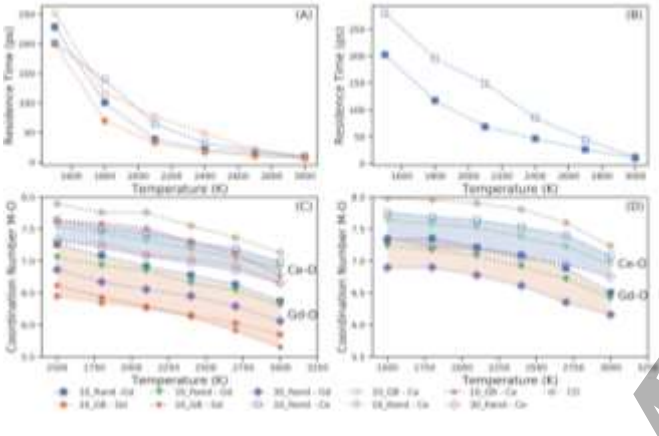


Figure 8: Residence time for oxygen with Gd and Ce cations as a function of temperature for the GB (A) and intergrain regions (B). Coordination number as a function of temperature for the GB (A) and intergrain regions (B). Data is presented for the Σ3(111) grain boundary.

### *3.5 Oxygen Diffusion at Grain Boundaries*

The presence of dopants was found to significantly increase the oxygen transport along the grain boundary. We illustrate this by showing a typical 1ns trajectory of 3 oxygen atoms (1 in the grain boundary and two in the GI) for three different grain boundary simulations, for example a time averaged density of diffusing species (oxygen) shows that in N_GB configurations, enhanced diffusion is localised to the grain boundary, with no change in diffusion in the grain interior when compared with the stoichiometric structure (Figure9A/B). In contrast, in N_Rand configurations there is significant diffusion in both the grain boundary and grain interior (Figure 9C). Both observations can be rationalised by examining the oxygen vacancy distribution. N_Rand configurations have a more uniform distribution of $V_o$, albeit with a higher concentration in the grain boundary, throughout the structure. This more even distribution of charge carriers facilitates diffusion throughout. In N_GB configurations $V_o$ have all localised in the grain boundary leaving few hopping sites in the grain interior, as it is for stoichiometric configurations.

As the grain interior and the grain boundary regions display such different behaviour, we treated the two regions separately. Considering the grain boundary regions for all the grain boundary configurations, our data does not show significant variation in the magnitude of the diffusivity (i.e. diffusion coefficient Figure S6 and S7). As the concentration of $Gd^{3+}$ increases, the diffusivity increases for all configurations.

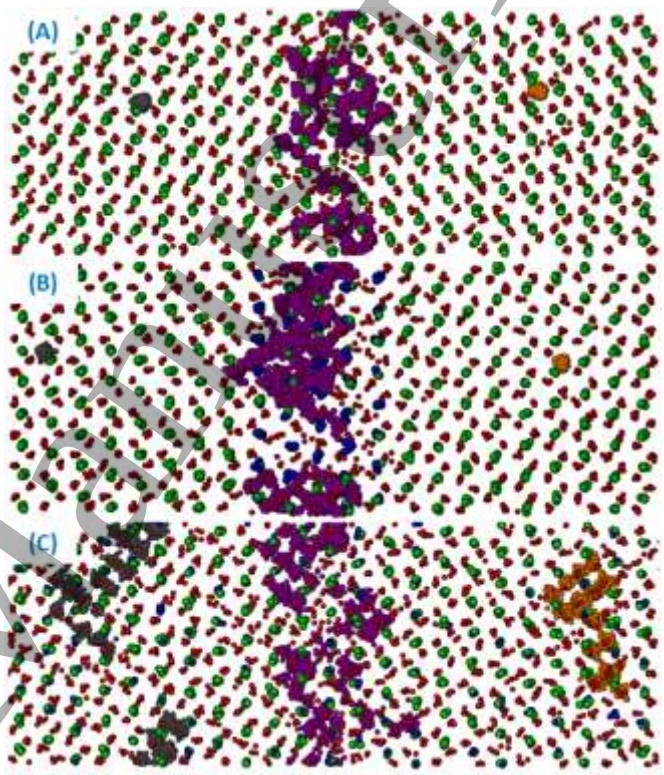


Figure 9: Shows the superimposition of a snapshot of the grain boundary and the grain interior regions of (A) stoichiometric (CO), (B) 10_GB and (C) 30_Rand Σ3(111) configurations. For clarity Oxygen, Cerium and Gadolinium are shown i n red, green and blue. To illustrate the effect of the grain boundary on diffusion, the full trajectory across 1 ns for a single oxygen atom has been shown for one oxygen in the grain boundary region (purple) and one in the grain interior either side of the boundary (grey and orange).

In the N_GB configurations (where all $Gd^{3+}$ are located in the grain boundary) there is only a small concentration of oxygen vacancies in the grain interior. For this reason, the activation energies for $V_o$ diffusion could not be reliably calculated in the grain interior regions for these configurations due to a lack of statistics. However, activation energies were able to be calculated in the grain interior regions of the 10, 16 and 30 N_Rand configurations, and are 0.8, 0.9 and 1.0 eV respectively. Grain boundary regions generally have a slightly increased activation energy

compared with the grain interior (Figure 10). The Σ3(111), Σ11(311), Σ5(210) and Σ9(221) N_Rand configurations have a similar but slightly larger activation energy at the GB compared with the GI regions whereas the Σ5(310) and Σ19(331) N_Rand configurations have a much larger activation energy in the GI regions compared with the GB. With the exception of the Σ19(331) grain boundary the N_Rand configurations have lower activation energies that the N_GB configurations. This highlights that the specific local micro-structure of these materials can have a large effect on transport properties. This is in line with experimental predictions that grain boundary regions reduce the conductivity of the material.

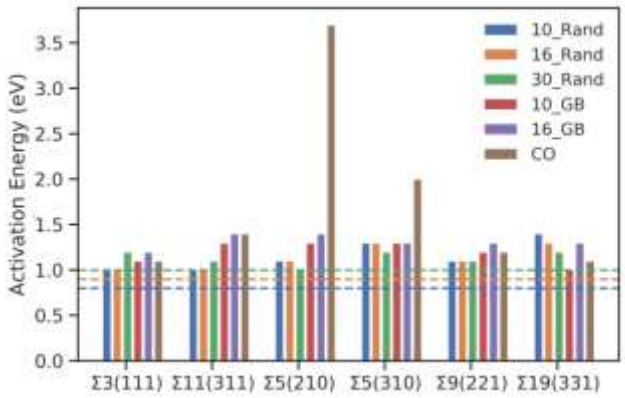


Figure 10: Activation energies for oxygen diffusion in the grain boundary regions for all the nanolayer configurations. The calculated GI activation energies for the 10_Rand, 16_Rand and 30_Rand are denoted by blue, orange and green horizontal lines.

The stoichiometric Σ5(210) has the highest activation energy, followed by the stoichiometric Σ5(310), indicating that these grain boundaries may be strongly blocking oxygen transport. However upon the introduction of dopants there is a large decrease in the Ea for both grain boundaries to values similar to all other grain boundaries.

A possible explanation for the low diffusivity in the Σ5 boundaries relates to the cation density at the boundary compared with the interboundary region. We find in the stoichiometric Σ3, Σ9, Σ11 and Σ19 boundaries there is a slight decrease in cation density, whereas in the Σ5 boundaries there is an increase in cation density (Figure 11). Upon introduction of impurities there is a decrease in the cation density at the boundary due to a slight widening of the boundary region (Figure 11b-c). The contribution of the cation density at the grain boundary to the transport properties of boundaries provides a possible explanation for the strong blocking nature of the stoichiometric Σ5.

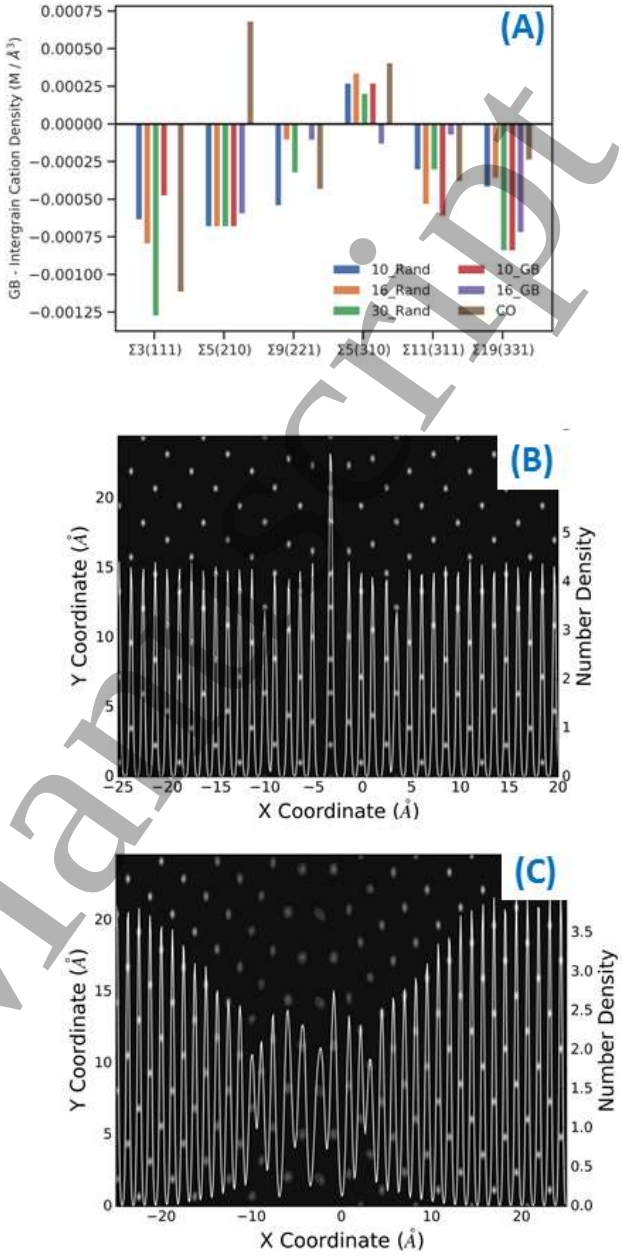


Figure 11: Cation density difference between the grain interior region and the grain boundary region for all configurations studied (A). Time averaged two dimensional density profiles of the centre of mass of both $Ce^{4+}$ and $Gd^{3+}$ displayed every 0.5ps at different temperatures, overlaid with the one dimensional cation density profile for the stoichiometric (B) and 16_GB GDC (C) Σ5 (210)

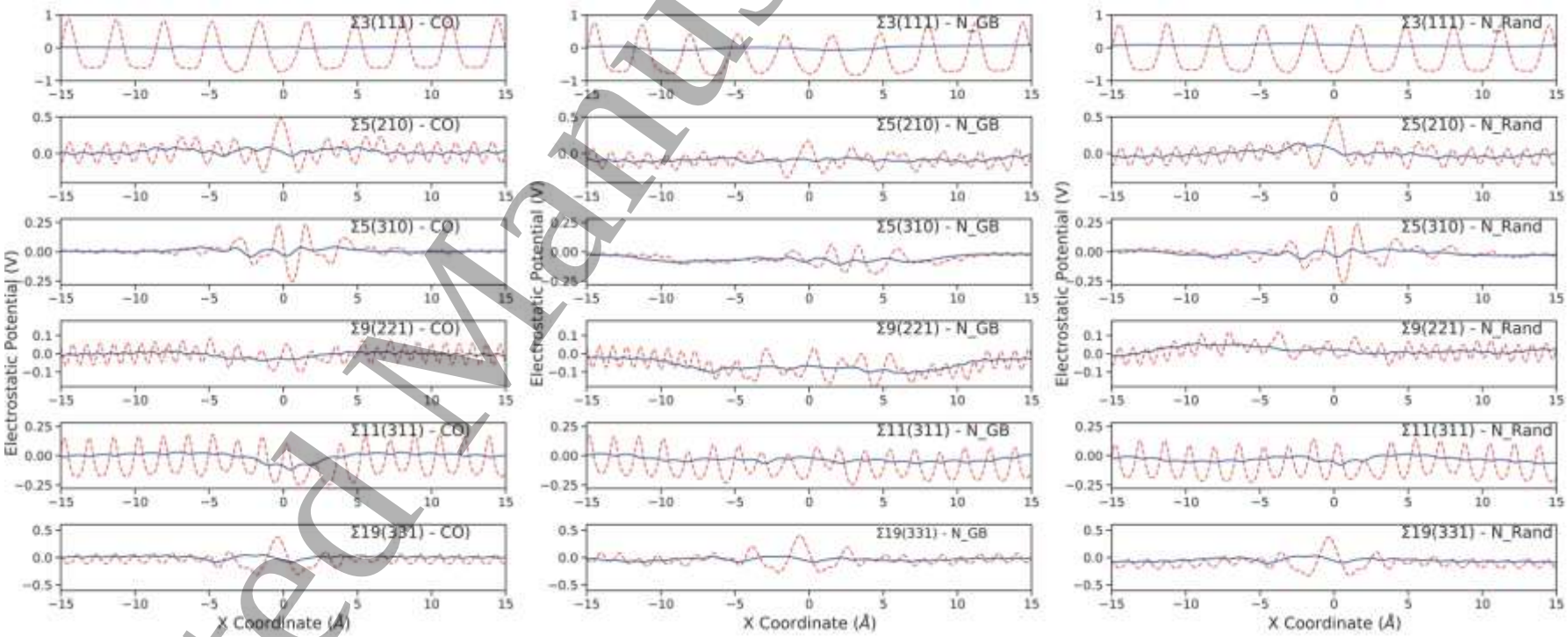


Figure 12 – Red dashed lines: Poisson potentials calculated from molecular dynamics simulations as a function of distance from the grain boundary plane (-15 - + 15Å) at 2100 K for the stoichiometric, 10_GB and 10_Rand configurations. Blue solid lines: running average potentials over one lattice spacing.

### *3.6 Electrostatic Potential at Grain Boundaries*

We have calculated the electrostatic potential as a function of distance either side (-15Å - +15Å) of the grain boundary core positioned at 0Å (Figure 12/13), for each grain boundary within each scheme (stoichiometric CO, doped grain boundary region (N_GB) and randomly doped grain boundary and grain interior regions (N_Rand)). The lattice polarization is illustrated by the X projection of the mean electrostatic potential (Figure 12 – red dashed line). The sharp oscillations along X are due to the oppositely charged planes of $Ce^{4+}/Gd^{3+}$ and $O^{2-}$. The polarization field is seen more clearly from a running average of the electrostatic potential, calculated across a distance equal to one lattice spacing (Figure 12 – blue solid line). Generally there are quite substantial differences between the profiles of different grain boundaries. Some structures show disruption of the electrostatic potential at the core of the grain boundary that extend into the grain interior; this is hardly visible in the Σ3(111) whereas it is significant in the Σ5(310).

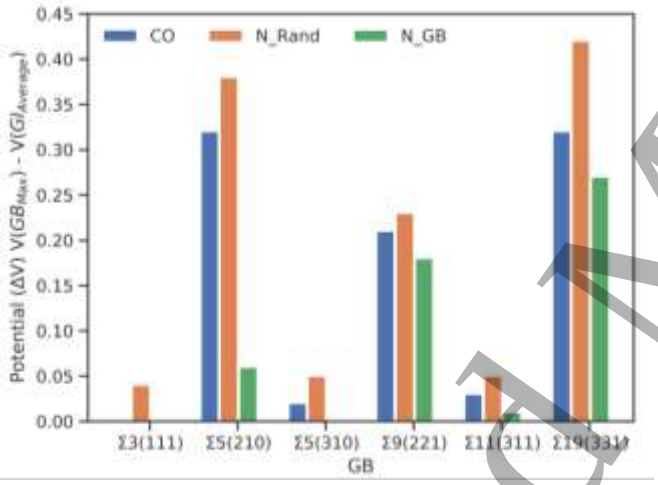


Figure 13 – Difference between the average electrostatic Poisson potential at the grain interior and at the grain boundary core for the stoichiometric CO (Blue), N_Rand (Orange) and N_GB (Green) configurations for all grain boundary structures.

We find that N_GB configurations have a slightly lower potential at the boundary relative to the stoichiometric structures (Figure 13), which is in contrast with the N_Rand configurations, which generally have a slightly larger potential. This is due to the distribution of oxygen vacancies within the systems. The N_Rand configurations have an constant distribution of $Gd^{3+}$ throughout but an uneven distribution of $V_o$ (i.e. the average Vo density is greater in the GI compared to the GB regions, Figure 7), thus there is a greater net positive charge at the GB relative to the GI. In contrast the N_GB configurations display segregation of both $Gd^{3+}$ and almost all $V_o$ at the grain boundaries, thus there is a reduction in charge density at the GB region relative to the grain interior and so the potential is smaller (Figure 13).

## 4. Discussion

We have demonstrated that we have a simple, robust approach for generating grain boundary structures, with a high throughput computational approach by putting together all possible surface terminations, scanning each surface relative to the other and at each site performing an energy minimisation. In this way we have generated realistic models of ceria coincidence site lattice (CSL) tilt grain boundaries, which are characteristic of the fluorite structure, [31-34, 38-43].

All calculations, both molecular mechanics and molecular dynamics, show that grain boundaries are sinks for gadolinium and oxygen vacancy segregation (Fig 4, 5 and 7), although the oxygen vacancies ($V_o$), segregation depends on GBs local structure. For example the Σ3(111) shows a small (0.06 eV) driving force for $V_o$ segregation, whereas the Σ5(310) has a larger segregation energy for $V_o$ (up to 0.5eV). This observation agrees with the findings of Dholabhai et al, where the defect energy is found to be sensitive to the local environment, i.e. the GB. [18] The segregation of $V_o$ was also found to be dependent on distance from the grain boundary core by Allen et al[44] to a depth of approximately 1.5nm. This is similar to that found from EELS, which revealed an enhanced oxygen vacancy and gadolinium concentration in first 2-4 nm from the GB and is assumed to be the effective width of the space charge layer. [13] For a information the reader can refer to more detailed papers. [12, 20]

A key result is that although grain boundaries are sinks for oxygen vacancies, dopant segregation may play a much greater role in their segregation. All N_GB configurations, where all $Gd^{3+}$ was segregated in the grain boundary regions see a complete depletion of $V_o$ in their grain interior regions (Figure 4), which is in line with previous experimental reports. [12, 45-47] Whereas in N_Rand configurations, where there is an equal amount of $Gd^{3+}$ in the grain interior, a significant amount of oxygen vacancies do not segregate to the grain boundary. We therefore speculate that as devices degrade over time and the $Gd^{3+}$ concentration decreases in the grain interior and increases in the grain boundaries, there will be a depletion of charge carriers in the grain interiors and thus an overall decrease in conductivity.

As there is accumulation of $V_o$ in the grain boundary, oxygen diffusion increases due to the increase of charge carriers. However, visual inspection has shown that this is limited to the GB region, hence the high oxygen diffusion

remains parallel to the grain boundary plane (Figure 9). Although the oxygen diffusion in GB regions is much higher than in the GI regions, the activation energies are higher due to the energy required for an oxygen to leave the coordination sphere of an already undercoordinated cation atom. A higher activation energy for oxygen diffusion in GB was measured by Avila-Paredes et al., for heavily Gd doped.[48] The activation energies for oxygen in our GI regions (Fig 9) are in line with experiments with heavily doped Gd samples (30%) having the highest Ea. As the dopant concentration decreases so does Ea. [49-52] We can comment on the blocking effect of grain boundaries in GDC within the context of our results. Generally this blocking behaviour has been quantitatively described using the space charge layer model, which sees a positive electrostatic potential at the grain boundary core due to segregation of oxygen vacancies and oxygen vacancy depletion (space charge layers SCL) adjacent to the core; this induces a reduction in ionic conductivity. [21, 52-54] It is energetically favourable for large quantities of $Gd^{3+}$ to segregate to the grain boundary, along with the majority of charge carriers ($V_o$). This depletion of charge carriers in the grain interiors results in the blocking effect of grain boundaries as diffusion is limited to the grain boundary planes (i.e. parallel to the GB plane). The simulated potential maps show this same behaviour for a number of grain boundaries, i.e. with a positive core potential along with depletion zones.

Positive space-charge potentials of 0.3V have been obtained for polycrystalline ceria which is in good agreement with some of those calculated for our grain boundaries. [55] Furthermore the blocking grain boundary effects depend also on temperature and the dopant content and type. [56-58] When the temperature is high enough, the grain boundary resistance appears to become negligible in comparison to the grain resistance, although this behaviour varies with dopant types and concentrations (usually 15 mol% regardless of the dopant type). Samples of heavily doped cerium oxides, prepared by Spark Plasma Sintering in the form of a high density (>98%) body with grain size of ~15nm, showed no grain boundary blocking effect and moreover the conductivity was demonstrated to be purely ionic.[10]

## 5. Conclusions

We have conducted simulations on two different GDC systems, namely N_GB (i.e. dopants segregated at the grain boundaries) which is an analogue for a degraded solid electrolyte of a SOFC device, and N_Rand (i.e. dopants randomly distributed between grain boundaries and grain interiors) which is an analogue for a freshly made material. We find that segregation of $Gd^{3+}$ to the grain boundaries is a thermodynamically favourable process and thus the N_Rand configurations will degrade into the N_GB configurations over time. Furthermore, as the oxygen vacancies are strongly attracted to $Gd^{3+}$ the resulting high concentrations of $Gd_2O_3$ at the N_GB grain boundaries lead to a reduction in grain interior oxygen transport and this transport is limited to the grain boundaries. Counter to this, we find that a more uniform distribution of $Gd^{3+}$ allows transport to occur in the grain interiors as well as in the grain boundaries as oxygen vacancies can also reside close to $Gd^{3+}$ dopants in the grain interior. Thus segregation of dopants over time is a significant factor in the blocking effect of grain boundaries in GDC, which we evaluated in terms of electrostatic potential.

## Acknowledgements

We would like acknowledge AWE and EPSRC (EP/P007821/1, EP/R010366/1, EP/R023603/1) for funding and Benjamin Morgan for useful conversations on this topic. Computations were run on Balena HPC facility at the University of Bath, the Orion computing facility at the University of Huddersfield and the ARCHER UK National Supercomputing Service (http://www.archer.ac.uk) via our membership of the UK's HEC Materials Chemistry Consortium (HEC MCC) funded by EPSRC (EP/L000202, EP/R029431).

## Author Contributions

ARS and MM carried out the simulations, ARS performed the data analysis, MM and SCP designed the study, ARS and MM wrote the manuscript with contributions from all authors.

## References

[1] Steele B C H 1996 Ceramic ion conducting membranes *Current Opinion in Solid State and Materials Science* **1** 684-91
[2] Inaba H and Tagawa H 1996 Ceria-based solid electrolytes *Solid State Ionics* **83** 1-16
[3] Park S, Vohs J M and Gorte R J 2000 Direct oxidation of hydrocarbons in a solid-oxide fuel cell *Nature* **404** 265-7
[4] Sunarso J, Baumann S, Serra J M, Meulenberg W A, Liu S, Lin Y S and Diniz da Costa J C 2008 Mixed ionic–electronic conducting (MIEC) ceramic-based membranes for oxygen separation *Journal of Membrane Science* **320** 13-41
[5] Kharton V V, Figueiredo F M, Navarro L, Naumovich E N, Kovalevsky A V, Yaremchenko A A, Viskup A P, Carneiro A, Marques F M B and Frade J R 2001 Ceria-based materials for solid oxide fuel cells *Journal of Materials Science* **36** 1105-17
[6] Steele B C H and Heinzel A 2001 Materials for fuel-cell technologies *Nature* **414** 345
[7] Steele B C H 2000 Appraisal of Ce1−yGdyO2−y/2 electrolytes for IT-SOFC operation at 500°C *Solid State Ionics* **129** 95-110
[8] Kilner J A and Burriel M 2014 Materials for Intermediate-Temperature Solid-Oxide Fuel Cells *Annual Review of Materials Research* **44** 365-93

[9] De Souza R A, Pietrowski M J, Anselmi-Tamburini U, Kim S, Munir Z A and Martin M 2008 Oxygen diffusion in nanocrystalline yttria-stabilized zirconia: the effect of grain boundaries *Physical Chemistry Chemical Physics* **10** 2067-72

[10] Anselmi-Tamburini U, Maglia F, Chiodelli G, Tacca A, Spinolo G, Riello P, Bucella S and Munir Z A 2006 Nanoscale Effects on the Ionic Conductivity of Highly Doped Bulk Nanometric Cerium Oxide *Advanced Functional Materials* **16** 2363-8

[11] Li Z-P, Mori T, Auchterlonie G J, Zou J and Drennan J 2011 Direct evidence of dopant segregation in Gd-doped ceria *Applied Physics Letters* **98** 093104

[12] Guo X and Waser R 2006 Electrical properties of the grain boundaries of oxygen ion conductors: Acceptor-doped zirconia and ceria *Progress in Materials Science* **51** 151-210

[13] Lei Y, Ito Y, Browning N D and Mazanec T J 2002 Segregation Effects at Grain Boundaries in Fluorite-Structured Ceramics *Journal of the American Ceramic Society* **85** 2359-63

[14] Kim S, Fleig J and Maier J 2003 Space charge conduction: Simple analytical solutions for ionic and mixed conductors and application to nanocrystalline ceria *Physical Chemistry Chemical Physics* **5** 2268-73

[15] Maier J 2005 Nanoionics: ion transport and electrochemical storage in confined systems *Nature Materials* **4** 805

[16] Gunn D S D, Allan N L and Purton J A 2014 Adaptive kinetic Monte Carlo simulation of solid oxide fuel cell components *Journal of Materials Chemistry A* **2** 13407-14

[17] Lee S S, Song W, Cho M, Puppala H L, Phuc N, Zhu H, Segatori L and Colvin V L 2013 Antioxidant Properties of Cerium Oxide Nanocrystals as a Function of Nanocrystal Diameter and Surface Coating *Acs Nano* **7** 9693-703

[18] Dholabhai P P, Aguiar J A, Wu L, Holesinger T G, Aoki T, Castro R H R and Uberuaga B P 2015 Structure and segregation of dopant–defect complexes at grain boundaries in nanocrystalline doped ceria *Physical Chemistry Chemical Physics* **17** 15375-85

[19] A.R.Symington M M, N.A.Brincat, N.R.Williams and S.C.Parker 2019 Defect Segregation Facilitates Oxygen Transport at Fluorite UO2 Grain Boundaries *Philosophical Transactions of the Royal Society of London. Series A:*

[20] De Souza R A 2009 The formation of equilibrium space-charge zones at grain boundaries in the perovskite oxide SrTiO3 *Physical Chemistry Chemical Physics* **11** 9939-69

[21] Maier J 1986 On the Conductivity of Polycrystalline Materials *Berichte der Bunsengesellschaft für physikalische Chemie* **90** 26-33

[22] Watson G W, Kelsey E T, deLeeuw N H, Harris D J and Parker S C 1996 Atomistic simulation of dislocations, surfaces and interfaces in MgO *Journal of the Chemical Society-Faraday Transactions* **92** 433-8

[23] Sayle T X T, Cantoni M, Bhatta U M, Parker S C, Hall S R, Mobus G, Molinari M, Reid D, Seal S and Sayle D C 2012 Strain and Architecture-Tuned Reactivity in Ceria Nanostructures; Enhanced Catalytic Oxidation of CO to CO2 *Chemistry of Materials* **24** 1811-21

[24] Sayle T X T, Molinari M, Das S, Bhatta U M, Mobus G, Parker S C, Seal S and Sayle D C 2013 Environment-mediated structure, surface redox activity and reactivity of ceria nanoparticles *Nanoscale* **5** 6063-73

[25] Williams N R, Molinari M, Parker S C and Storr M T 2015 Atomistic investigation of the structure and transport properties of tilt grain boundaries of UO2 *Journal of Nuclear Materials* **458** 45-55

[26] Galmarini S, Aschauer U, Bowen P and Parker S C 2008 Atomistic Simulation of Y-Doped α-Alumina Interfaces *Journal of the American Ceramic Society* **91** 3643-51

[27] Tasker P W and Duffy D M 1984 The structure and properties of the stepped surfaces of MgO and NiO *Surface Science* **137** 91-102

[28] Smith W and Forester T R 1996 DL_POLY_2.0: A general-purpose parallel molecular dynamics simulation package *Journal of Molecular Graphics* **14** 136-41

[29] Kerisit S and Parker S C 2004 Free energy of adsorption of water and metal ions on the [1014] calcite surface *J Am Chem Soc* **126** 10152-61

[30] Morgan B J and Madden P A 2012 Absence of a space-charge-derived enhancement of ionic conductivity in β|γ-heterostructured 7H- and 9R-AgI *Journal of Physics: Condensed Matter* **24** 275303

[31] Nerikar P V, Rudman K, Desai T G, Byler D, Unal C, McClellan K J, Phillpot S R, Sinnott S B, Peralta P, Uberuaga B P and Stanek C R 2011 Grain Boundaries in Uranium Dioxide: Scanning Electron Microscopy Experiments and Atomistic Simulations *Journal of the American Ceramic Society* **94** 1893-900

[32] Shibata N, Ikuhara Y, Oba F, Yamamoto T and Sakuma T 2002 Atomic structure and solute segregation of a Σ = 3, [110]/{111} grain boundary in an yttria-stabilized cubic zirconia bicrystal *Philosophical Magazine Letters* **82** 393-400

[33] Shibata N, Oba F, Yamamoto T and Ikuhara § Y 2004 Structure, energy and solute segregation behaviour of [110] symmetric tilt grain boundaries in yttria-stabilized cubic zirconia *Philosophical Magazine* **84** 2381-415

[34] Fisher C A J and Matsubara H 1999 The influence of grain boundary misorientation on ionic conductivity in YSZ *Journal of the European Ceramic Society* **19** 703-7

[35] Feng B, Yokoi T, Kumamoto A, Yoshiya M, Ikuhara Y and Shibata N 2016 Atomically ordered solute segregation behaviour in an oxide grain boundary *Nature Communications* **7** 11079

[36] Zha S, Xia C and Meng G 2003 Effect of Gd (Sm) doping on properties of ceria electrolyte for solid oxide fuel cells *Journal of Power Sources* **115** 44-8

[37] Minervini L, Zacate M O and Grimes R W 1999 Defect cluster formation in M2O3-doped CeO2 *Solid State Ionics* **116** 339-49

[38] Fisher C A J and Matsubara H 1999 Molecular dynamics investigations of grain boundary phenomena in cubic zirconia *Computational Materials Science* **14** 177-84

[39] Fisher C A J and Matsubara H 1998 Oxide ion diffusion along grain boundaries in zirconia: A molecular dynamics study *Solid State Ionics* **113-115** 311-8

[40] Shibata N, Yamamoto T, Sakuma T and Ikuhara Y 2001 Structure of [110] tilt grain boundaries in zirconia bicrystals *Journal of Electron Microscopy* **50** 429-33

[41] Shibata N, Morishige N, Yamamoto T, Ikuhara Y and Sakuma T 2002 Stacking-fault formation in [001] small-angle symmetric tilt grain boundaries in cubic zirconia bicrystals *Philosophical Magazine Letters* **82** 175-81

[42] Dickey E C, Fan X and Pennycook S J 2001 Structure and Chemistry of Yttria-Stabilized Cubic-Zirconia Symmetric Tilt Grain Boundaries *Journal of the American Ceramic Society* **84** 1361-8

[43] Mao Z, Sinnott S B and Dickey E C 2002 Ab Initio Calculations of Pristine and Doped Zirconia Σ5 (310)/[001] Tilt Grain Boundaries *Journal of the American Ceramic Society* **85** 1594-600

[44] Allen J P, Greń W, Molinari M, Arrouvel C, Maglia F and Parker S C 2009 Atomistic modelling of adsorption and segregation at inorganic solid interfaces *Molecular Simulation* **35** 584-608

[45] Göbel M C, Gregori G and Maier J 2012 Electronically blocking grain boundaries in donor doped cerium dioxide *Solid State Ionics* **215** 45-51

[46] Guo X, Sigle W, Fleig J and Maier J 2002 Role of space charge in the grain boundary blocking effect in doped zirconia *Solid State Ionics* **154-155** 555-61

[47] Maier J 2014 Pushing Nanoionics to the Limits: Charge Carrier Chemistry in Extremely Small Systems *Chemistry of Materials* **26** 348-60

[48] Avila-Paredes H J, Choi K, Chen C-T and Kim S 2009 Dopant-concentration dependence of grain-boundary conductivity in ceria: A space-charge analysis *Journal of Materials Chemistry* **19** 4837-42

[49] Ruiz-Trejo E, Sirman J D, Baikov Y M and Kilner J A 1998 Oxygen ion diffusivity, surface exchange and ionic conductivity in single crystal Gadolinia doped Ceria *Solid State Ionics* **113-115** 565-9

[50] Zhang F, Chan S W, Spanier J E, Apak E, Jin Q, Robinson R D and Herman I P 2002 Cerium oxide nanoparticles: Size-selective formation and structure analysis *Applied Physics Letters* **80** 127-9

[51] Pérez-Coll D and Mather G C 2010 Electrical transport at low temperatures in dense nanocrystalline Gd-doped ceria *Solid State Ionics* **181** 20-6

[52] Guo X, Sigle W and Maier J 2003 Blocking Grain Boundaries in Yttria-Doped and Undoped Ceria Ceramics of High Purity *Journal of the American Ceramic Society* **86** 77-87

[53] Chiang Y M, Lavik E B, Kosacki I, Tuller H L and Ying J Y 1996 Defect and transport properties of nanocrystalline CeO2−x *Applied Physics Letters* **69** 185-7

[54] Göbel M C, Gregori G, Guo X and Maier J 2010 Boundary effects on the electrical conductivity of pure and doped cerium oxide thin films *Physical Chemistry Chemical Physics* **12** 14351-61

[55] Kim S and Maier J 2002 On the Conductivity Mechanism of Nanocrystalline Ceria *Journal of the Electrochemical Society* **149** J73-J83

[56] Hong S J, Mehta K and Virkar A V 1998 Effect of Microstructure and Composition on Ionic Conductivity of Rare-Earth Oxide-Doped Ceria *Journal of the Electrochemical Society* **145** 638-47

[57] GERHARDT R and NOWICK A S 1986 Grain-Boundary Effect in Ceria Doped with Trivalent Cations: I, Electrical Measurements *Journal of the American Ceramic Society* **69** 641-6

[58] Wang D Y and Nowick A S 1980 The "grain-boundary effect" in doped ceria solid electrolytes *Journal of Solid State Chemistry* **35** 325-33